Article:
Sabet, S.A. and Borst, R. (2019) Structural softening, mesh dependence, and regularisation in non-associated plastic flow. International Journal for Numerical and Analytical Methods in Geomechanics, 43 (13). pp. 2170-2183. ISSN 0363-9061

https://doi.org/10.1002/nag.2973

ORIGINAL ARTICLE

International Journal for Numerical and Analytical Methods in Geomechanics

Structural softening, mesh dependence, and regularisation in non-associated plastic flow

Sepideh Alizadeh Sabet[1] | **René de Borst**[1]

[1]Department of Civil and Structural Engineering, The University of Sheffield, Sheffield, S1 3JD, UK

Correspondence
René de Borst, Department of Civil and Structural Engineering, The University of Sheffield, Sheffield, S1 3JD, UK
Email: r.deborst@sheffield.ac.uk

Funding information
H2020 European Research Council, Grant Number: 664734 "PoroFrac"

A severe dependence of numerical simulations on the mesh density is usually attributed to the presence of strain softening in the constitutive relation. However, other material instabilities, like non-associated plastic flow, can also cause mesh sensitivity. Indeed, loss of ellipticity in quasi-static analyses is the fundamental cause of the observed mesh dependence. It has been known since long that non-associated plastic flow can cause loss of ellipticity, but the consequence for mesh sensitivity, and subsequently, for the difficulty of the equilibrium-finding iterative procedure to converge, have remained largely unnoticed. We first demonstrate at the hand of a biaxial test structural softening and a marked mesh dependence for an ideally-plastic material equipped with a non-associated flow rule. The phenomena are then analysed in depth using an infinitely long shear layer. Finally, it is shown that the mesh effect disappears when the standard continuum model is replaced by a Cosserat continuum, a well-known regularisation method for strain-softening constitutive relations.

KEYWORDS
Non-associated plasticity, mesh dependence, regularisation, Cosserat continuum, ellipticity

1 | INTRODUCTION

In the 1980s it was observed that the introduction of strain softening in constitutive relations caused a phenomenon now known as mesh dependence or mesh sensitivity. While it is normal that, upon refinement of the discretisation, the numerical solution approaches the correct solution of the initial value problem, the connotations mesh dependence or mesh sensitivity are typically reserved for a phenomenon where the solution does not seem to converge to the correct solution, or at least, a solution is found which does not seem physically realistic. This is most simply shown at the hand of a one-dimensional bar loaded in tension and composed of a strain softening material. Upon refinement of the discretisation, the post-peak descending branch runs steeper and steeper, giving a more and more brittle structural response. Beyond a certain number of elements a snap-back phenomenon is observed, and the overall displacement decreases after passing the peak load. In the limit of an infinitely dense mesh the post-peak load-displacement curve doubles back on its original (elastic) loading branch, resulting in the physically unrealistic case of failure without energy dissipation [1].

While this phenomenon has originally been ascribed to shortcomings of the finite element formulation, the true reason appeared to be the loss of well-posedness of the initial or boundary-value problem, and thus emerges for *any* discretisation method [2, 3]. Indeed, for quasi-static problems ellipticity ceases to hold at a certain stage of the loading process and failure takes place at a discrete, characteristic plane, where the governing equations have turned hyperbolic. The observed mesh dependence is then just a manifestation of the inability of the discretisation method to exactly capture a discrete plane. Various regularisation methods have been proposed to locally avoid losing ellipticity, including non-local or gradient continua, micromorphic (Cosserat) continua, and the inclusion of viscosity and rate effects [4].

It has been recognised that strain softening is not the only material instability which can lead to loss of ellipticity. Indeed, it has also been demonstrated for strain-*rate* softening [5], while seminal analyses by Mandel [6], Rudnicki and Rice [7], Needleman [8] and others [9, 10] have shown that non-associated flow also has a materially destabilising effect and can lead to a local loss of ellipticity, thus causing the boundary-value problem to become ill-posed. In principle, non-associated flow can therefore also induce structural softening and mesh sensitivity, but with some exceptions [11, 12], little attention has been given in the literature to the possibility of this phenomenon to occur.

Herein, we will first recall that the introduction of a non-associated flow in plasticity can induce structural softening. We will do this at the hand of shear banding in a biaxial test. To focus on non-associated flow as the sole destabilising effect, strain softening and possible geometrical destabilising effects have been excluded from the analysis. This example will also serve to illustrate how mesh dependence typically manifests itself in non-associated plasticity, which is often different from how it appears in simulations which involve strain softening. However, the underlying mathematical reason, namely the loss of ellipticity, is the same for both instability phenomena, and it will be briefly recalled how non-associated flow can cause loss of ellipticity. Next, the case of a shear layer in pure shear will be examined in detail, analytically and numerically, regarding the occurrence of mesh dependence and structural softening caused by non-associated plastic flow. The ill-posedness of the boundary-value problem induced by the loss of ellipticity is normally remedied by the introduction of a localisation limiter, or regularisation method. As stated above, a number of methods exist, and the Cosserat continuum [13, 14, 15, 16] has been suggested as an approach that can be physically well motivated for granular materials. After a succinct summary of the elasto-plastic Cosserat continuum, the shear layer is reanalysed with this enriched continuum model, and the results are shown to be mesh objective, yet still exhibiting structural softening.

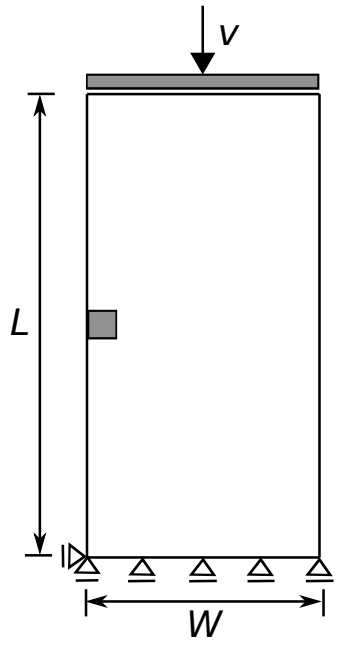

FIGURE 1 Biaxial test with boundary conditions and imperfection

2 | MESH DEPENDENCE IN NON-ASSOCIATED PLASTICITY

To demonstrate that in the absence of strain softening and geometrically destabilising effects, non-associated plastic flow can lead to structural softening and mesh dependence we study shear banding in a biaxial test. A Mohr-Coulomb yield surface has been adopted and the analyses have been carried out under plane-strain conditions.

2.1 | Non-associated Mohr-Coulomb plasticity

We consider a linear elastic-perfectly plastic Mohr-Coulomb model. Ordering the principal stress such that σ_1 is the smallest and σ_3 is the largest principal stress, the Mohr-Coulomb yield function is given by:

$$f = \frac{1}{2}(\sigma_3 - \sigma_1) + \frac{1}{2}(\sigma_3 + \sigma_1)\sin\phi - c\cos\phi \tag{1}$$

with c and ϕ the cohesion and the angle of internal friction, respectively. For non-associated flow the yield function f is augmented by a plastic potential function

$$g = \frac{1}{2}(\sigma_3 - \sigma_1) + \frac{1}{2}(\sigma_3 + \sigma_1)\sin\psi \tag{2}$$

with $\psi \leq \phi$ being the dilatancy angle, from which the plastic strain rates can be derived:

$$\dot{\boldsymbol{\varepsilon}}^p = \dot{\lambda}\frac{\partial g}{\partial \boldsymbol{\sigma}} \tag{3}$$

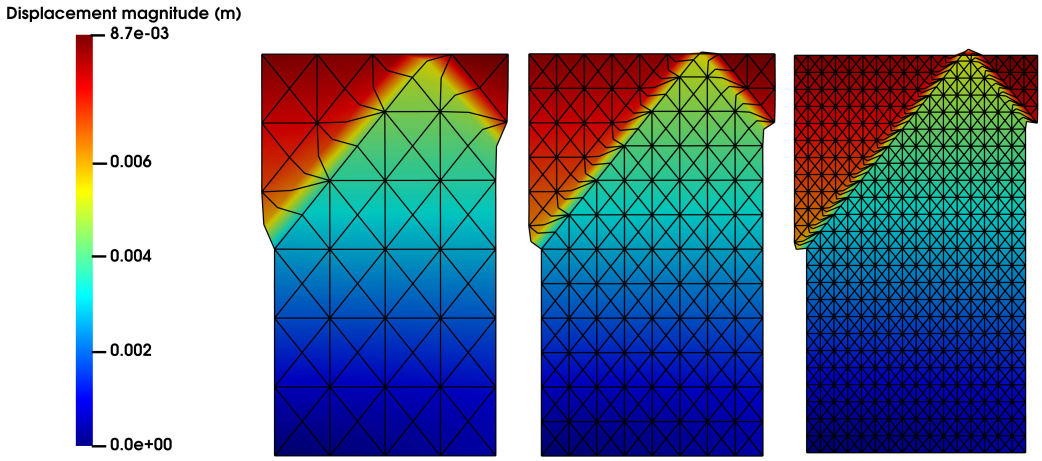

FIGURE 2 Deformed contours for the biaxial test

For the implementation of the non-associated Mohr-Coulomb model, reference is made to the literature [1], including the construction of a consistent tangent operator, which has been used in the analysis, and a proper treatment of stresses near the apex of the yield cone.

2.2 | Shear banding in a biaxial test: mesh dependence

Calculations have been carried out with the elastic-ideally plastic Mohr-Coulomb model for the geometry of Figure 1. Three different meshes have been used, depicted in Figure 2 with 6-noded triangular elements in a crossed lay-out. The dimensions of the specimen are $L = 2$ m and $W = 1$ m. The Young's modulus is $E = 1000$ Pa, Poisson's ratio $\nu = 0.2$, cohesion $c = 1$ Pa, angle of internal friction $\phi = 20^{\circ}$ and dilatancy angle $\psi = 10^{\circ}$. At the left boundary one element, just above the centre, has been given a 5% reduction in cohesive strength. The nodes at the bottom are rollers with the exception of the left-bottom corner node, which is also fixed in the horizontal direction. Uniform displacements are prescribed at the top to give a compressive stress field.

Figure 2 shows that localised shear bands develop and that upon mesh refinement the localisation bands become narrower and narrower. This points to a vanishing width in the limit of an infinitely dense mesh, which is associated with loss of ellipticity. Mesh dependence is also shown in the load-displacement diagram of Figure 3, in particular when we consider the zoom. However, different from the mesh dependence encountered when using strain-softening constitutive relations, the mesh dependence only shows up in the first part after the peak load has been reached, and levels out to reach the same *residual* load. Importantly, the results confirm earlier analyses that non-associated flow rules can induce *structural softening*, even though the constitutive relation does not feature strain softening [11, 12].

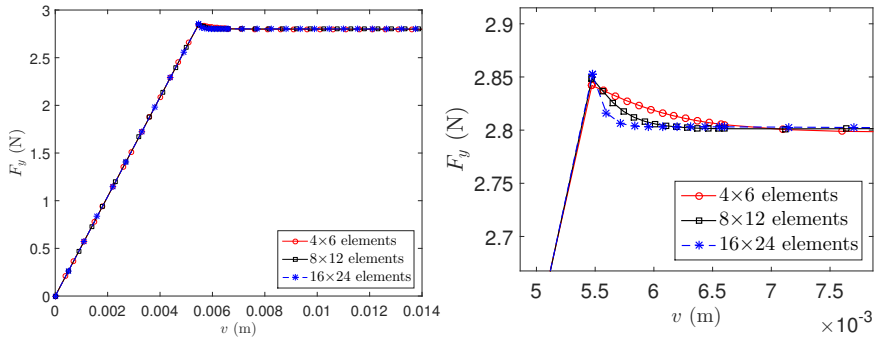

(a) Full curve (b) Zoom post peak

FIGURE 3 Load *vs* displacement for the biaxial test

3 | THE UNDERLYING CAUSE: LOSS OF ELLIPTICITY

Considering quasi-static loading conditions, the governing differential equations – equilibrium equations, kinematic equations and constitutive equations – normally have an elliptic character. Mathematically, this implies that discontinuities in the solution are not possible. Now suppose that within the given context of quasi-static loading conditions, a (possibly curved) plane emerges, say Γ_d, across which the solution is possibly discontinuous. The difference in the traction rate $\dot{\mathbf{t}}_d$ across this plane reads:

$$[\![\dot{\mathbf{t}}_d]\!] = \mathbf{n}_{\Gamma_d} \cdot [\![\dot{\boldsymbol{\sigma}}]\!] \tag{4}$$

with $\mathbf{n}_{\Gamma_d}$ the normal vector to the discontinuity Γ_d, or using the constitutive relation $\dot{\boldsymbol{\sigma}} = \mathbf{D} : \dot{\boldsymbol{\epsilon}}$, with $\mathbf{D}$ the tangential stiffness tensor

$$[\![\dot{\mathbf{t}}_d]\!] = \mathbf{n}_{\Gamma_d} \cdot \mathbf{D} : [\![\dot{\boldsymbol{\epsilon}}]\!] \tag{5}$$

where the assumption of a linear comparison solid [17] has been introduced, i.e. $\mathbf{D}$ is assumed to have the same value at both sides of the discontinuity Γ_d.

A velocity field $\dot{\mathbf{u}}$ that is crossed by a single discontinuity can be represented as:

$$\dot{\mathbf{u}} = \dot{\tilde{\mathbf{u}}} + \mathcal{H}_{\Gamma_d} \dot{\hat{\mathbf{u}}} \tag{6}$$

with the Heaviside function $\mathcal{H}_{\Gamma_d}$ separating the continuous velocity fields $\dot{\tilde{\mathbf{u}}}$ and $\dot{\hat{\mathbf{u}}}$. The strain rate field is obtained by straightforward differentiation:

$$\dot{\boldsymbol{\epsilon}} = \nabla^{\text{sym}} \dot{\tilde{\mathbf{u}}} + \mathcal{H}_{\Gamma_d} \nabla^{\text{sym}} \dot{\hat{\mathbf{u}}} + \delta_{\Gamma_d} (\dot{\hat{\mathbf{u}}} \otimes \mathbf{n}_{\Gamma_d})^{\text{sym}} \tag{7}$$

where the superscript 'sym' denotes the symmetrised part of the operator and δ_{Γ_d} is the Dirac function at Γ_d. The

difference in strain rate fields at Γ_d is proportional to the unbounded term at the interface:

$$[\![\dot{\boldsymbol{\epsilon}}]\!] = \zeta \left(\dot{\mathbf{u}} \otimes \mathbf{n}_{\Gamma_d}\right)^{\text{sym}} \tag{8}$$

with ζ a non-zero scalar. Substitution into Equation (5) gives:

$$[\![\dot{\mathbf{t}}_d]\!] = \zeta \left(\mathbf{n}_{\Gamma_d} \cdot \mathbf{D} \cdot \mathbf{n}_{\Gamma_d}\right) \cdot \dot{\mathbf{u}} \tag{9}$$

where the minor symmetry of the tangential stiffness tensor has been exploited. A non-trivial solution can exist if and only if the determinant of the acoustic tensor vanishes:

$$\det \left(\mathbf{n}_{\Gamma_d} \cdot \mathbf{D} \cdot \mathbf{n}_{\Gamma_d}\right) = 0 \tag{10}$$

If this condition, Eq. (10), is met, discontinuous solutions can emerge and loss of ellipticity of the governing differential equations occurs. It is noted that Eq. (10) is coincident with Hill's condition for the propagation of plane acceleration waves in solids [18].

For a Mohr-Coulomb plasticity model with a non-associated flow rule used in the previous section, it has been shown that the criterion of Eq. (10) results in a critical hardening modulus h_{crit} at which ellipticity is lost, and hence shear bands can develop [6, 10]:

$$\frac{h_{\text{crit}}}{\mu} = \frac{(\sin\phi - \sin\psi)^2}{8(1-\nu)} \tag{11}$$

with μ and ν the shear modulus and Poisson's ratio, respectively. Since $\mu > 0$ and $\nu \leq 1/2$, loss of ellipticity already occurs for positive values of the hardening modulus h in the case of non-associated flow, i.e. when $\psi < \phi$. For non-hardening plasticity $h = 0$, and consequently, $h < h_{\text{crit}}$, implying that the governing equations are not elliptic, and that mesh sensitive solutions can emerge.

4 | A CLOSER LOOK: ANALYSIS OF A SHEAR LAYER

To investigate the structural softening and mesh dependence encountered in the shear-band simulation of the biaxial test in more detail, we consider the simpler case of a shear layer under plane-strain conditions, which is infinitely long in the horizontal x-direction. The discretised shear layer is amenable to an analytical solution, which we will compare with a numerical simulation for different mesh densities.

4.1 | Analytical solution

We assume that the shear layer is sub-divided into m elements (constant strain). One element has a marginally lower shear strength than the other $m-1$ elements and will therefore plasticise, while the remaining elements unload. For this element, the shear strain can be decomposed as:

$$\gamma = \gamma^e + \gamma^p \tag{12}$$

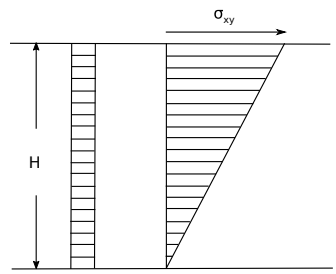

FIGURE 4 An infinitely long shear layer

With τ the shear stress and μ the shear modulus, so that $\gamma^e = \tau/\mu$, we can rewrite Eq. (12) as:

$$\gamma = \frac{\tau}{\mu} + \gamma^p \tag{13}$$

We adopt a Drucker-Prager yield function,

$$f = \sqrt{3J_2} + \alpha^* p - k^* \tag{14}$$

with the material parameters α^* and k^* related to the cohesion c and the angle of internal friction, ϕ. Considering plane-strain conditions, Eq. (14) reduces to:

$$f = \tau + \alpha p - k \tag{15}$$

under pure shear loading, where

$$\alpha = \frac{2\sqrt{3}\sin\phi}{3-\sin\phi} \quad , \quad k = \frac{2\sqrt{3}c\cos\phi}{3-\sin\phi} \tag{16}$$

In a standard manner, a plastic potential function is introduced:

$$g = \tau + \beta p \tag{17}$$

where β is related to the dilatancy angle ψ similar to the relation between α and ϕ in Eq. (16). The plastic shear and volumetric strain rates then directly follow as:

$$\begin{cases} \dot{\gamma}^p = \dot{\lambda}\frac{\partial g}{\partial \tau} = \dot{\lambda} \\ \dot{\epsilon}_v^p = \dot{\lambda}\frac{\partial g}{\partial p} = \dot{\lambda}\beta \end{cases} \tag{18}$$

which results in the dilatancy relation:

$$\dot{\gamma}^p = \frac{\dot{\epsilon}_v^p}{\beta} \tag{19}$$

and for proportional loading:

$$\gamma^p = \frac{\epsilon_v^p}{\beta} \tag{20}$$

With the additive decomposition for the volumetric strain:

$$\epsilon_v = \epsilon_v^e + \epsilon_v^p \tag{21}$$

Eq. (19) becomes:

$$\gamma^p = \frac{\epsilon_v - \epsilon_v^e}{\beta} \tag{22}$$

Since $\epsilon_v^e = p/\kappa$, with κ the bulk modulus, we can rewrite Eq. (22) as:

$$\gamma^p = \frac{\epsilon_v}{\beta} - \frac{p}{\beta\kappa} \tag{23}$$

and Eq. (13) becomes:

$$\gamma = \frac{\tau}{\mu} - \frac{p}{\beta\kappa} + \frac{\epsilon_v}{\beta} \tag{24}$$

Since the yield condition must hold during progressive yielding, i.e. $f = 0$, we have from Eq. (15):

$$p = \frac{k - \tau}{\alpha} \tag{25}$$

and Eq. (24) becomes:

$$\gamma = \frac{\tau}{\mu} + \frac{\tau - k}{\alpha\beta\kappa} + \frac{\epsilon_v}{\beta} \tag{26}$$

We assume that all m elements have an equal length, h. For the total height of the layer we thus have $H = mh$. There are two possible assumptions for ϵ_v.

Case I: We assume that $\epsilon_v = 0$ on a pointwise basis, in this case for each (constant strain) element. Numerically, this can be realised by preventing each element from displacing vertically. Eq. (26) then reduces to:

$$\gamma = \frac{\tau}{\mu} + \frac{\tau - k}{\alpha\beta\kappa} \tag{27}$$

Noting that only in the weakened element we have elasto-plastic deformations, and the remaining $m - 1$ elements feature only elastic strains, the horizontal displacement at the top of the layer reads:

$$u = \gamma h + (m - 1)h\frac{\tau}{\mu} \tag{28}$$

or using Eq. (27):

$$u = mh\frac{\tau}{\mu} + h\frac{\tau - k}{\alpha\beta\kappa} \tag{29}$$

Hence, the average shear strain over the layer becomes:

$$\bar{\gamma} = \frac{u}{H} = \frac{\tau}{\mu} + \frac{\tau - k}{m\alpha\beta\kappa} \tag{30}$$

Eq. (30) shows that there is a clear mesh dependence since, when increasing m, the response becomes more brittle. When $\tau \downarrow 0$, we have an inverse dependence on the numbers of elements:

$$\lim_{\tau\to 0} \bar{\gamma} = -\frac{k}{m\alpha\beta\kappa} \tag{31}$$

We note that $\alpha \geq 0$ and $\kappa > 0$, but that for plastic contraction $\beta < 0$. For $\tau \downarrow 0$, we therefore have $\bar{\gamma} > 0$.

Case II: The condition of incompressibility $\epsilon_v = 0$ is not imposed pointwise, but over the entire shear layer. This implies that part of the plastic expansion/contraction in the failing element can be compensated by elastic volumetric strains in the other elements. Numerically, this condition can be simulated by only prescribing roller boundary conditions at the top of the layer together with linear dependence (master-slave) relations to ensure that nodes on the same horizontal line displace the same amount. It is noted that when imposing this condition, the other $(m-1)$ elements may satisfy the yield condition at some point.

Let the additional shear strain be denoted by $\Delta\gamma$. Then, the additional horizontal displacements at the top of the layer is

$$\Delta = \Delta\gamma^w h + (m-1)\Delta\gamma^l h \tag{32}$$

where the superscripts w and l denote the weak element and the remainder of the layer, respectively. Substitution of Eq.(13) then gives:

$$\frac{\Delta u}{h} = \frac{\Delta\tau}{\mu} + (\Delta\gamma^p)^w + (m-1)\left(\frac{\Delta\tau}{\mu} + (\Delta\gamma^p)^l\right) \tag{33}$$

Use of the dilatancy relation, Eq. (20), subsequently gives:

$$\frac{\Delta u}{h} = m\frac{\Delta\tau}{\mu} + \frac{1}{\beta}\left((\Delta\epsilon_v^p)^w + (m-1)(\Delta\epsilon_v^p)^l\right) \tag{34}$$

Exploiting the additive decomposition of the strain into an elastic and a plastic component, and considering that the shear layer deforms isochorically, we obtain:

$$\frac{\Delta u}{h} = m\frac{\Delta\tau}{\mu} - \frac{1}{\beta}\left((\Delta\epsilon_v^e)^w + (m-1)(\Delta\epsilon_v^e)^l\right) \tag{35}$$

Since the stresses are on the yield surface, the consistency condition holds holds for a finite increment:

$$\Delta p = -\frac{\Delta\tau}{\alpha} \tag{36}$$

so that:

$$(\Delta\epsilon_v^e)^w = (\Delta\epsilon_v^e)^l = \frac{\Delta p}{\kappa} = -\frac{\Delta\tau}{\alpha\kappa} \tag{37}$$

Substitution into Eq. (35) then yields:

$$\Delta\bar{\gamma} = \frac{\Delta u}{H} = \frac{\Delta\tau}{\mu} + \frac{\Delta\tau}{\alpha\beta\kappa} \tag{38}$$

giving a slope:

$$\frac{d\bar{\gamma}}{d\tau} = \frac{1}{\mu} + \frac{1}{\alpha\beta\kappa} \tag{39}$$

Physically, α, μ and κ must be positive. However, $\beta < 0$ for plastic contraction, and, depending on the precise values of α, β, μ and κ, we have $\frac{d\bar{\gamma}}{d\tau} < 0$, leading to structural softening. However, since m has dropped out of the expression, there is no mesh dependence under the current assumption.

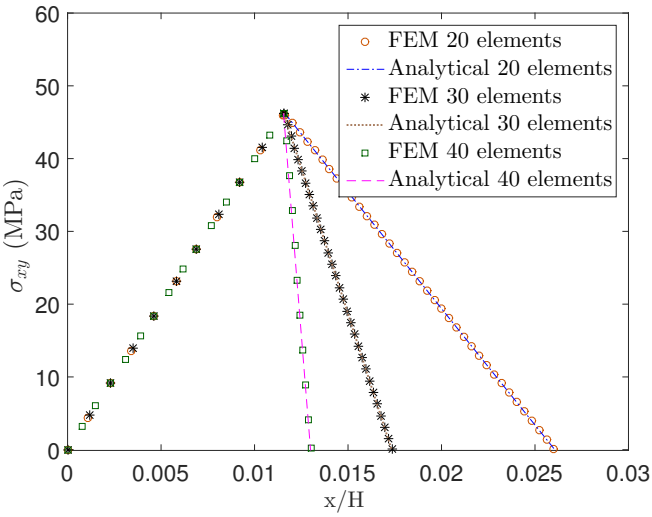

FIGURE 5 Load-displacement curves for Case I of the infinitely long shear layer

4.2 | Numerical solutions

We first consider Case I, and analyse a layer with a height $H = 100$ mm. The material parameters have been taken as Young's modulus $E = 10000$ MPa and Poisson's ratio $\nu = 0.25$, while for the plasticity the following values have been used: $\alpha = 0.2$, $\beta = -0.2$ and $k = 100$ MPa, with the latter parameter reduced by 20% for the weaker element. Three mesh densities have been used, with 20, 30 and 40 elements, respectively. The load-displacement curves have been plotted in Figure 5 along with the corresponding analytical solutions, cf. Eq. (30). The numerical results fully coincide with the analytical solution.

For all discretisations a clear structural softening is observed, which is in keeping with the numerical solutions

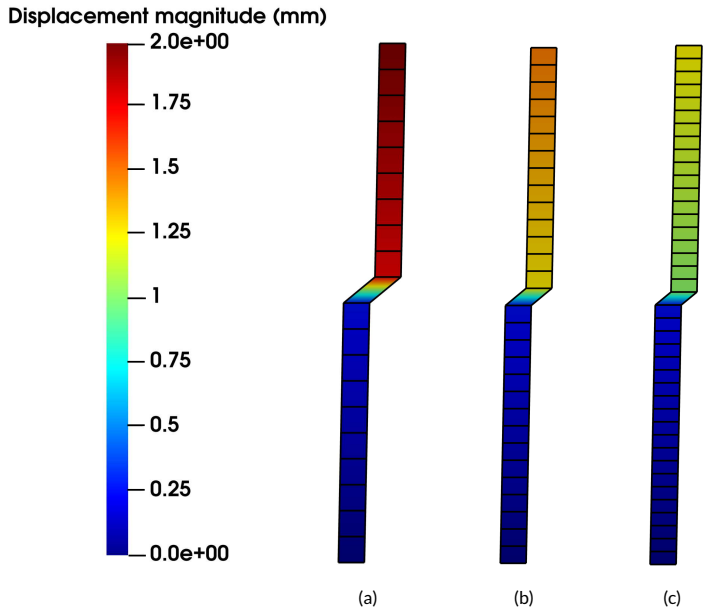

FIGURE 6 Deformed model for Case I, at $\tau = 20$ MPa, using a standard Drucker-Prager model

obtained for the biaxial test just after reaching the peak load, Figure 3. Moreover, the mesh dependence observed in the biaxial test, i.e. for finer meshes the descending branch of the post-peak load-displacement curve becomes steeper, is also corroborated by the numerical and analytical results for the shear layer. Even more visible than in the biaxial test, see Figure 2, it is now apparent that localisation is confined to a single element (layer), see Figure 6, which shows the deformed contours of the shear layer beyond peak load at $\tau = 20$ MPa.

We next consider case II, with again three different discretisations, but now with 20, 40 and 80 elements, respectively. As with Case I, there is a clear structural softening, see Figure 7. However, the numerical and analytical solutions only match after progressive deformations, and then indeed do not exhibit any mesh dependence, as predicted by the analytical solution of Eq. (39). The discrepancy between the analytical solution and the numerical results is due to the fact that the assumption is violated that there are no plastic strains outside the weaker element. Because of the occurrence of plastic straining outside the weak element right after the peak load the numerical results there also become slightly mesh dependent, as shown in the zoom. At progressive overall displacements the plastic zone again becomes confined to the weaker element and the assumption underlying the analytical solution is satisfied. Figure 8 shows the deformed contours at a residual shear stress level $\tau = 43$ MPa. As with the previous case, localisation is confined to a single element, irrespective of the number of elements used to model the shear layer.

5 | COSSERAT ELASTO-PLASTICITY

The structural softening and mesh dependence which have been encountered in the preceding examples is due to a local loss of ellipticity of the governing set of partial differential equations. As has been stated in the Introduction, this can be prevented by using a non-Boltzmann continuum model or by introducing rate dependence. Herein we investigate

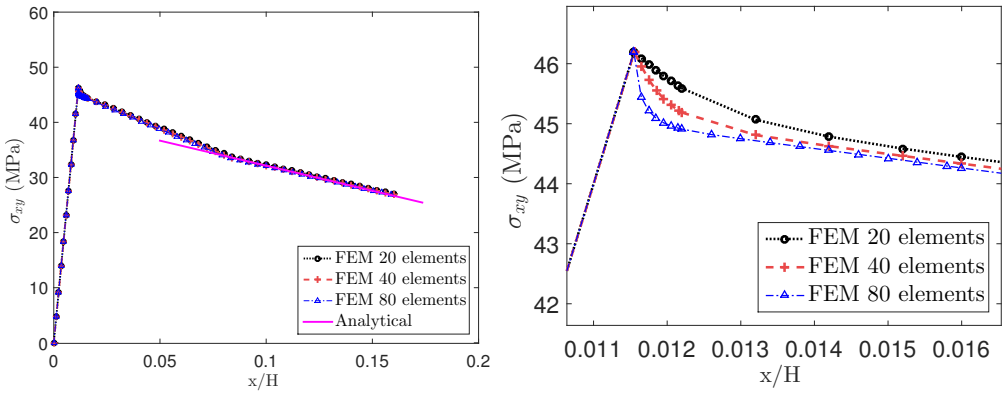

(a) Full diagram

(b) Zoom post peak

FIGURE 7 Load vs displacement for Case II of the infinitely long shear layer

whether the use of a Cosserat continuum model, which has been popular for describing geomaterials [13] and has been shown to be effective in removing mesh dependence due to strain softening [14, 15, 16], can be an effective localisation limiter for non-associated flow as well.

5.1 | Model formulation

Neglecting inertia terms and body forces linear and rotational equilibrium of a Cosserat continuum can be formulated as [19, 20]:

$$\operatorname{div} \boldsymbol{\sigma}^{\mathsf{T}} = 0 \tag{40}$$

and

$$\operatorname{div} \mathbf{m}^{\mathsf{T}} + \boldsymbol{e} : \boldsymbol{\sigma} = 0 \tag{41}$$

respectively, where $\boldsymbol{\sigma}$ is the Cauchy stress tensor, $\mathbf{m}$ is the couple-stress tensor, and $\boldsymbol{e}$ is the permutation tensor. Conjugate to the Cauchy stress tensor and the couple-stress tensor are the strain tensor $\boldsymbol{\epsilon}$ and the micro-curvature tensor $\boldsymbol{\kappa}$, which are derived from the usual displacement vector $\mathbf{u}$ and a micro-rotation vector $\boldsymbol{\omega}$, as follows:

$$\boldsymbol{\epsilon} = \nabla \mathbf{u} - \boldsymbol{e} \cdot \boldsymbol{\omega} \tag{42}$$

and

$$\boldsymbol{\kappa} = \nabla \boldsymbol{\omega} \tag{43}$$

For a small-strain elasto-plastic Cosserat continuum the usual additive decomposition of the strain tensor into an

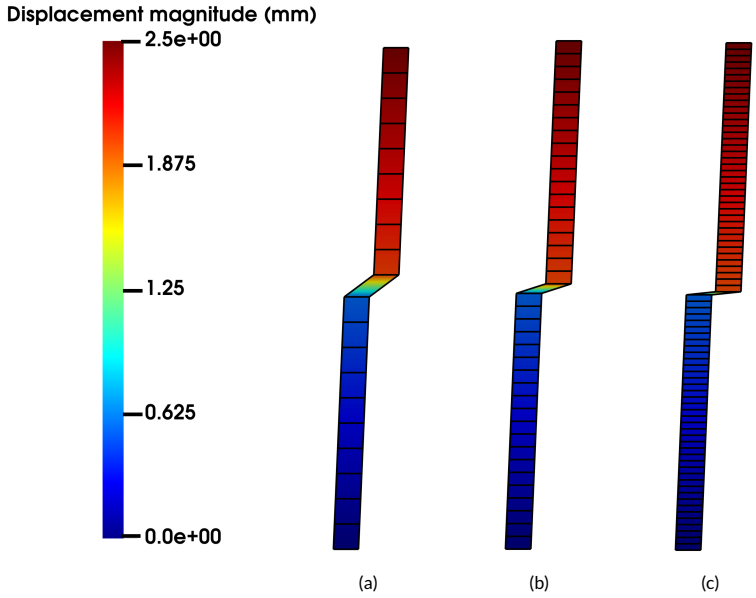

FIGURE 8 Deformed contours for Case II, at $\tau = 43$ MPa using a standard Drucker-Prager model

elastic and a plastic part is assumed,

$$\boldsymbol{\epsilon} = \boldsymbol{\epsilon}^e + \boldsymbol{\epsilon}^p \tag{44}$$

augmented with a similar relation for the micro-curvatures:

$$\boldsymbol{\kappa} = \boldsymbol{\kappa}^e + \boldsymbol{\kappa}^p \tag{45}$$

The elastic parts of the strain and the micro-curvature tensors are linearly related to the stress and couple-stress tensors, as follows

$$\boldsymbol{\sigma} = \frac{2\nu\,\mu\,\mathrm{tr}(\boldsymbol{\epsilon}^e)}{1-2\nu}\,\mathbf{I} + (\mu+\mu_c)\,\boldsymbol{\epsilon}^e + \mu\,(\boldsymbol{\epsilon}^e)^{\mathsf{T}} \tag{46}$$

and

$$\mathbf{m} = \mu\left(\ell_1^2\,\boldsymbol{\kappa}^e + \ell_2^2\,(\boldsymbol{\kappa}^e)^{\mathsf{T}} + \ell_3^2\,\mathrm{tr}(\boldsymbol{\kappa}^e)\,\mathbf{I}\right) \tag{47}$$

where $\mathbf{I}$ is the second-order unit tensor, and μ_c, ℓ_1, ℓ_2 and ℓ_3 are additional material parameters. For planar deformations, the last two terms in the expression for $\mathbf{m}$ cancel, and we have the reduced expression

$$\mathbf{m} = \mu\ell^2\,\boldsymbol{\kappa}^e \tag{48}$$

with $\ell_1 = \ell$ introducing an internal length in the enhanced continuum model, which sets the width of the localisation zone.

A non-associated Drucker-Prager type perfect-plasticity model is considered which is appropriate for geomaterials showing friction. The yield criterion is as in Eq. (14), but with the second invariant of deviatoric stresses generalised as [13]:

$$J_2 = a_1\, \mathbf{s}^{\mathsf{T}} : \mathbf{s} + a_2\, \mathbf{s} : \mathbf{s} + a_3\, \mathbf{m}^{\mathsf{T}} : \mathbf{m}/\ell^2 \tag{49}$$

where s_{ij} are the components of the deviatoric stress tensor, and $a_1 + a_2 = \frac{1}{2}$. In this paper the values of $a_1 = \frac{1}{4}$, $a_2 = \frac{1}{4}$ and $a_3 = \frac{1}{2}$ are adopted as this will lead to a particularly simple numerical algorithm [14, 16]. The plastic potential takes a similar form as the yield function, cf. Eq. (14), but with a dilatancy factor, β^*, replacing the friction coefficient α^*:

$$g = \sqrt{3J_2} + \beta^* p \tag{50}$$

As in classical plasticity, the flow rule is derived from the plastic potential, cf. Eq. (3), and sets the plastic strain rate.

5.2 | Numerical solution for the shear layer

The material parameters used for the Cosserat Drucker-Prager model have been kept the same as those used in the classical Drucker-Prager model. Regarding the two additional parameters needed for planar deformations, we have assumed that $\mu_c = 2000$ MPa, while two values have been adopted for the characteristic length, namely $\ell = 2$ mm and $\ell = 5$ mm. The results of an analysis of the shear layer for Case I, but now using the Cosserat continuum, are discussed below.

The load-displacement curves in Figures 9(a) and 9(b) show that the results are now mesh independent, in the sense that they converge to a unique, physically realistic solution upon mesh refinement, which is different from the computations for the standard Drucker-Prager non-associated plasticity model. We emphasise that the introduction of the internal length scale ℓ, however, does not remove structural softening. Indeed, the internal length scale not only controls the width of the localisation zone, cf. Figures 10 and 11, but also the slope of the load-deformation curve. For a lower value of ℓ a more brittle post-peak behaviour occurs.

Case II was also reanalysed using the Cosserat continuum, and showed similar results as the computations for Case I. While the analysis of mesh dependence is not relevant now, the results continue to exhibit structural softening for the chosen set of material parameters. And like for Case I, but different from the results for the classical continuum, a width of the localisation zone appears which is independent of the discretisation for sufficiently dense meshes.

6 | CONCLUDING REMARKS

Numerical simulations using plasticity models with a non-associated flow rule embedded in a classical (Boltzmann) continuum show that structural softening can occur in spite of the fact that no explicit strain softening is applied to the cohesion or to the angle of internal friction [11, 12]. Moreover, a dependence of the solution on the fineness of the discretisation emerges, but the extent depends on the precise boundary value problem. In most cases the mesh dependence only manifests itself for a limited deformation range beyond the peak load, and mesh effects level out on progressive deformation, and a unique residual load is usually attained, independent of the discretisation.

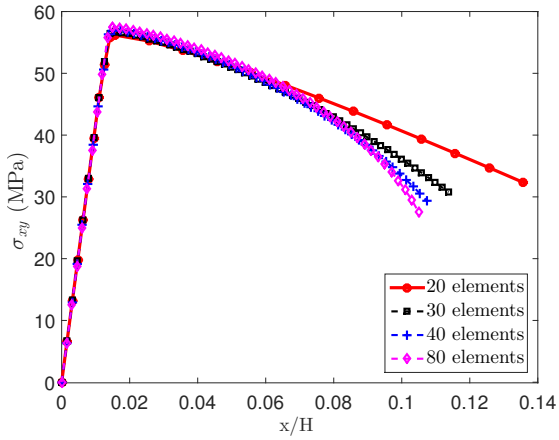

(a) l = 5 mm

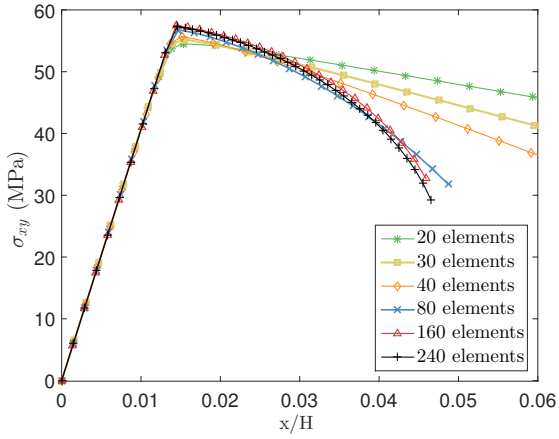

(b) l = 2 mm

FIGURE 9 Load-displacement curves for Case I, using a Cosserat Drucker-Prager model

The underlying reason of the mesh sensitivity is the loss of ellipticity, which occurs at a certain stage of the loading process when using a non-associated flow rule, and occurs even though strain softening is not included explicitly in the constitutive model, with the displacement gradients remaining infinitesimal [6, 7, 8, 10].

The Cosserat continuum can be exploited to remedy this deficiency [13, 19, 20], as it introduces an internal length scale. Indeed, numerical simulations show that the localisation zone then remains finite, and that load-displacements curves converge to a unique solution upon mesh refinement. The slope of the post-peak load-displacement curve and the width of the localisation zone are then set by the internal length scale. It is emphasised though, that structural softening is not removed by the regularisation, as has been demonstrated numerically.

The use of an enhanced continuum to prevent loss of ellipticity of quasi-static calculations (or loss of hyperbolicity in dynamic calculations) not only has implications for mesh sensitivity. It also has consequences for computability as the global convergence behaviour of the non-linear solver can be improved dramatically. Computations with non-associated flow rules are known to exhibit poor convergence, especially when the difference between the angle of internal friction

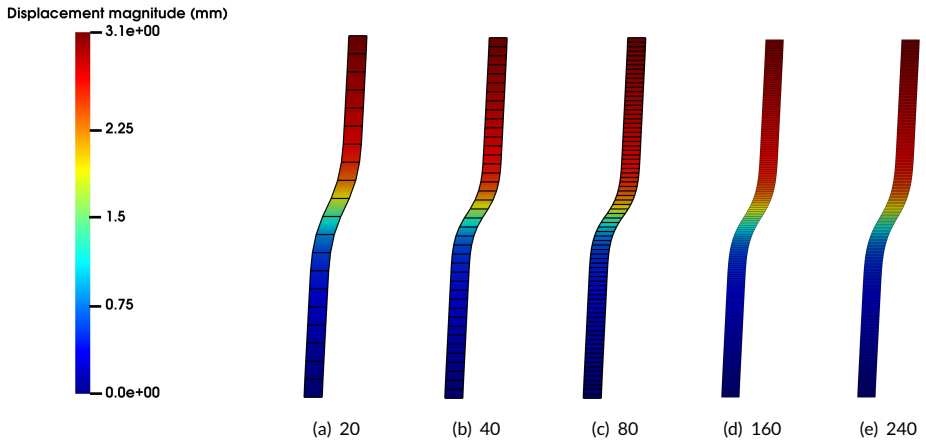

FIGURE 10 Deformed contours for Case I, with $\ell = 2$ mm, at $u = 3.1$ mm, using Cosserat Drucker-Prager model

and the dilatancy angle become bigger. This has often been attributed to the non-symmetry of the tangential stiffness matrix and the ensuing possible ill-conditioning. However, the computations herein suggest, and this has come out strongly in recent large-scale computations where viscoplasticity was used as regularisation method in non-associated plasticity [21], that it is actually the loss of ellipticity, and the ensuing ill-posedness of the initial value problem which causes the convergence issues in the iterative solver for the non-linear problem, rather than the non-symmetry of the tangential stiffness matrix. The use of a regularisation method in non-associated plasticity therefore not only improves the mesh sensitivity, but is also hugely beneficial for computability.

Evidently, the two issues are related. Indeed, strains are now no longer localised in a single element, but are distributed over a finite width. Increasing the resolution therefore does not lead to an increase of the strains locally, which can cause serious numerical issues. Examples are local snap-backs in the elasto-plastic return mapping procedure and the occurrence of multiple, non-physical equilibrium states, which can cause divergence of the global equilibrium-finding iterative procedure.

ACKNOWLEDGEMENTS

Financial support of the European Research Council under Advanced Grant 664734 “PoroFrac” is gratefully acknowledged.

REFERENCES

[1] de Borst R, Crisfield MA, Remmers JJC, Verhoosel CV. Non-Linear Finite Element Analysis of Solids and Structures. Second ed. Chichester: Wiley; 2012.

[2] Read HE, Hegemier GA. Strain softening of rock, soil and concrete – a review article. Mechanics of Materials 1984;3:271–294.

[3] Pamin J, Askes H, de Borst R. Two gradient plasticity theories discretized with the element-free Galerkin method. Computer Methods in Applied Mechanics and Engineering 2003;192:2377–2407.

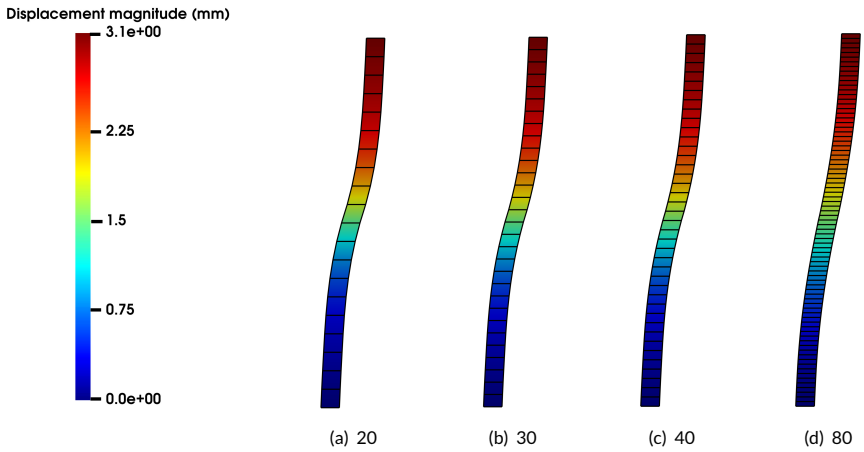

FIGURE 11 Deformed contours for Case I, with $\ell = 5$ mm, at $u = 3.1$ mm, using a Cosserat Drucker-Prager model

[4] de Borst R, Sluys LJ, Mühlhaus HB, Pamin J. Fundamental issues in finite element analysis of localisation of deformation. Engineering Computations 1993;10:99–122.

[5] Wang WM, Sluys LJ, de Borst R. Viscoplasticity for instabilities due to strain softening and strain-rate softening. International Journal for Numerical Methods in Engineering 1997;40:3839–3864.

[6] Mandel J. Conditions de stabilité et postulat de Drucker. In: Proceedings IUTAM Symposium on Rheology and Soil Mechanics Berlin: Springer-Verlag; 1966. p. 58–68.

[7] Rudnicki JW, Rice JR. Conditions for the localization of deformation in pressure sensitive dilatant materials. Journal of the Mechanics and Physics of Solids 1975;23:371–394.

[8] Needleman A. Non-normality and bifurcation in plane strain tension and compression. Journal of the Mechanics and Physics of Solids 1979;27:231–254.

[9] Vardoulakis I. Shear band inclination and shear modulus of sand in biaxial tests. International Journal for Numerical and Analytical Methods in Geomechanics 1980;4:103–119.

[10] Vermeer PA. The orientation of shear bands in biaxial tests. Géotechnique 1990;40:223–234.

[11] de Borst R. Bifurcations in finite element models with a non-associated flow law. International Journal for Numerical and Analytical Methods in Geomechanics 1988;12:99–116.

[12] Le Pourhiet L. Strain localization due to structural softening during pressure sensitive rate independent yielding. Bulletin de la Société géologique de France 2013;184:357–371.

[13] Mühlhaus HB, Vardoulakis I. The thickness of shear bands in granular materials. Géotechnique 1987;37:271–283.

[14] de Borst R. Simulation of strain localization: A reappraisal of the Cosserat continuum. Engineering Computations 1991;8:317–332.

[15] de Borst R, Sluys LJ. Localisation in a Cosserat continuum under static and dynamic loading conditions. Computer Methods in Applied Mechanics and Engineering 1991;90:805–827.

[16] de Borst R. A generalisation of J2-flow theory for polar continua. Computer Methods in Applied Mechanics and Engineering 1993;103:347–362.

[17] Hill R. A general theory of uniqueness and stability in elastic-plastic solids. Journal of the Mechanics and Physics of Solids 1958;6:236–249.

[18] Hill R. Acceleration waves in solid. Journal of the Mechanics and Physics of Solids 1962;10:1–16.

[19] Schaefer H. Das Cosserat-Kontinuum. Zeitschrift für Angewandte Mathematik und Mechanik 1967;47:485–498.

[20] Altenbach H, Eremeyev VA. Cosserat media. In: Generalized Continua – From the Theory to Engineering Applications Wien - Heidelberg - New York - Dordrecht - London: Springer-Verlag; 2013.p. 65–130.

[21] Duretz T, de Borst R, Le Pourhiet L. On finite thickness of shear bands in frictional viscoplasticity, and implications for lithosphere dynamics. Geochemistry, Geophysics, Geosystems 2019;(submitted).